

Multiple populations of extrasolar gas giants

SHOHEI GODA¹ AND TARO MATSUO¹

¹Department of Earth and Space Science, Graduate School of Science, Osaka University, 1-1, Machikaneyamacho, Toyonaka, Osaka 560-0043, Japan

(Received January 15, 2019; Revised January 15, 2019; Accepted January 15, 2019)

Submitted to ApJ

ABSTRACT

Statistically verifying the character of exoplanets, we can expect to reveal the formation or evolution processes of planetary systems. The notable parameters of planetary systems are metallicity of host star, planet mass, and eccentricity. Gas giants around metal rich stars are easily formed by core accretion. Since these planets are grown with bottom up, the distributions of planet masses and eccentricities are seemed to be continuously extended. On the other hand, the planetary formation by disk instability depends on mass and effective temperature of protoplanetary disk, but there is no strongly dependence on metallicity of host star. As these planets are not formed with bottom up, the planetary masses and eccentricities ununiformly distribute. In this study, we statistically revealed the planetary distributions of metal-rich and -poor regions, and tried to understand the planetary-formation and -evolution processes. Note that we made the dataset included the both selection biases of planetary detection for metal-rich and -poor regions to ignore the effect of these biases. As the results from classification for those samples with Gaussian Mixture Model, we found that the planetary distribution was divided into 3 regions by the boundaries around 3 and 13 M_J. We also discovered the different distributions of planet mass between each metallicity region, which explains the different processes of the planetary formation: core accretion model is applied in metal-rich region, and several formation models including core accretion are match in metal-poor region. In addition, we found that the distributions of planetary eccentricity have a difference between each mass cluster, especially in metal-rich region, which implies that there are dynamical interactions after the planets formed by core accretion.

Keywords: methods: data analysis – planets and satellites: terrestrial planets

1. INTRODUCTION

Decades ago, the discussion of planetary formation in solar system was developed (Hayashi et al. 1985), and two formation scenarios for Jupiter was proposed. One is core accretion (Perri & Cameron 1974; Mizuno 1980; Pollack et al. 1996) and another is disk instability (Kuiper 1951; Boss 1997; Mayer et al. 2002). In theory, the two planetary-formation processes have different dependences on disk metallicity, which is ratio of metal-density-number to hydrogen atoms, and planet mass (e.g., Matsuo et al. 2007). For core accretion model, since a protoplanet core needs to grow to the critical core mass before the disk gas dissipates, it easily occurs in the metal-rich region promoting the growth (Ida & Lin 2004b; Mordasini et al. 2012). **Actually, the detection probability for a planet around a metal-rich star is**

high (e.g., Santos et al. 2003; Fischer & Valenti 2005). **Although planets under 30 M_J can be formed through core accretion** (Tanigawa & Tanaka 2016), **the number of planets is decreasing with more massive. In addition, a massive planet has high eccentricity. The observational reports** (Ribas & Miralda-Escudé 2007; Santos et al. 2017; Schlaufman 2018) **show that there are two regions in a planetary distribution.** On the other hand, there are various reports about the relationship between disk metallicity and disk instability; there exists reports of correlation (Cai et al. 2006; Durisen et al. 2007), a very weak positive correlation (Mayer et al. 2007), and no correlation (Boss 2002) between disk metallicity and disk instability in the metallicity range of the stars hosting the observed planets.

Since the first planet around a normal star was discovered in 1995 (Mayor & Queloz 1995), by the large-

sized radial velocity observations, it was revealed that the amount of metallicity in a planetary system having small planets is less than having gas giants (Mayor et al. 2011; Wang & Fischer 2015). It seems that almost all gas giants are formed via core accretion because the central star and its surrounding protoplanetary disk are composed with the same molecular cloud (Ida & Lin 2004b; Mordasini et al. 2012).

The planetary-formation theories showed previous studies are based on the observed data, whose distributions are assumed to be close to real model. However, are there only two regions divided by the boundary of planet mass in a planetary distribution shown in the previous studies? This is because they discussed the planetary distribution without considering the effect of the selection bias. Some data was obtained with poor accuracy or short time observation, which include the bias depended on the metallicity. Since these poor observations restrict the detection possibility for planets, the distribution of discovered planets possibly include some underpopulated regions due to the selection bias. Furthermore, the previous studies insist that under 4 M_J planets are formed by core accretion, and over 4 M_J planets are explained by disk instability, but it is possible to form the massive planets under 30 M_J through core accretion in theory (e.g., Mordasini et al. 2009; Tanigawa & Tanaka 2016).

In this paper, since the radial velocity observation can detect the planetary masses or orbital eccentricities with good accuracy, we focus the dataset observed by radial velocity, and discuss the two planetary-formation processes for the planetary distribution, considering the selection biases. We explain how we analyze the planetary distribution, and select samples used in this study in Section 2. After that, we show the results obtained from the method of Section ??, and classify the planetary distribution in Section 3. Finally, we discuss the planetary-formation and -evolution processes from the results.

2. METHOD

In this section, we show the method of our study with two steps, and explain how we prepare the planet samples for this study.

2.1. Overview

まず最初に、主星の金属量に依存する選択効果の影響について考察していく。そのために、各々の金属量領域の選択効果を反対の領域に存在する惑星データにかけ、選択効果による影響を合わせたデータを作成していく (図を参照)。When a planetary system is observed, the upper limit of semi-major axis, $a|_{max}$, and lower limit of planet

mass, $M_p \sin i|_{min}$, in the system can be estimated with the accuracy of observation, σ , and observational term, τ as below (Torres et al. 2008),

$$a|_{max} = M_*^{\frac{1}{3}} \tau^{\frac{2}{3}}, \quad (1)$$

$$M_p \sin i|_{min} = 4.919 \times 10^{-3} P^{\frac{1}{3}} (1 - e)^{\frac{1}{2}} M_*^{\frac{2}{3}} \sigma, \quad (2)$$

where, M_* , P , and e are the star mass, orbital period, and eccentricity of planet, respectively. これらの値は各惑星系で異なり、特に金属量の値に依存した選択効果を生じる (図を参照)。また、惑星データを分けるための境界金属量を決定するために、様々な境界金属量で分けた2つの惑星サンプルを比較していく。この時、2つの分布が最も異なる場合を採用するため、AD検定を用いてそのp値が最小となる境界金属量を求めていく。そうして求めた境界金属量で惑星データを改めて分割し、各金属量領域に存在する惑星の軌道長半径および惑星質量の分布を比較し、分布に違いが見られるかを確認していく。その結果は Section 3.1 で示す。

続いて、選択効果による影響を合わせた惑星データを用いて、惑星分布を分類するための境界惑星質量を求めていく。本研究では分布の分類器として GMM, which can classify the extracted samples into several clusters, given that each cluster distributes a Gaussian function (e.g., Lee et al. 2012; Santos et al. 2017; Schlaufman 2018) を用い、主星の金属量と下限惑星質量の分布に対し分類を行う。そして分類された惑星データの軌道長半径と軌道離心率の分布を作成し、各領域でどのような分布の違いが見られるかを評価していく。その結果は Section 3.2 で示す。

First, we determined the boundary of metallicity, which makes the two divided planetary-mass distributions as most different, to verify the possibility of the effect due to the selection biases, and compared the two regions. Changing the metallicity boundary from -0.7 to 0.4 dex, we made the two regions' dataset, and evaluated the planetary-mass distributions with Anderson-Darling (AD) test. Note that we extracted randomly the values of planetary parameters considered their errors, and filtered each sample with any selection biases to remove the calculation bias. Then, the simulations were iterated until the value of boundary was settled. As the result, we found that the best border of metallicity is -0.09 dex. Dividing data with this border, we compared the planetary-mass distributions of both regions. The left of Figure 3, (a) shows the relation between semi-major axes and planetary mass, and the right one is the cumulative of planetary mass. AD test for the metal-rich and -poor regions showed that the p-value is 5.6×10^{-5} , which can low enough to dismiss the two samples. Thus, we proposed that there is no effect of selection biases for planetary distribution, and exists a difference between the each metallicity region.

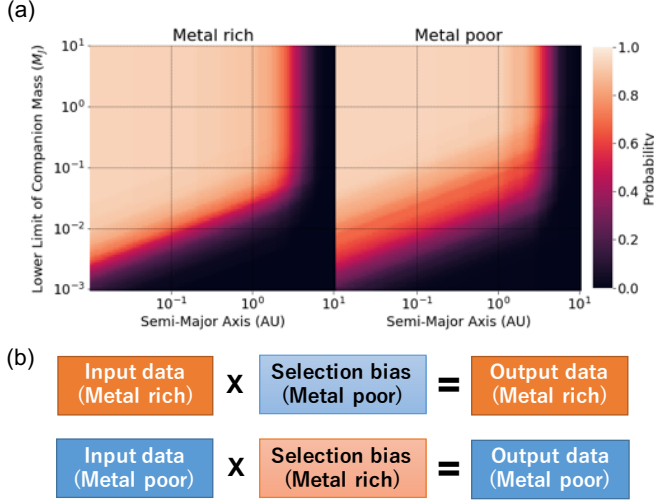


Figure 1. (a) Detectable regions for metal-rich (left) and -poor systems (right). The boundary of metallicity was fixed to 0.0 dex. Each planetary system is observed by the radial velocity measurements with each detection probability. (b) Method for equalizing the two selection biases in two different metallicity regions. The planetary distribution is additionally filtered with the opposite selection bias to remove the different selection biases in the two metallicity regions.

When a planetary system is observed, the upper limit of semi-major axis, $a|_{max}$, and lower limit of planet mass, $M_p \sin i|_{min}$, in the system can be estimated with the accuracy of observation, σ , and observational term, τ as below (Torres et al. 2008),

$$a|_{max} = M_*^{\frac{1}{3}} \tau^{\frac{2}{3}}, \quad (3)$$

$$M_p \sin i|_{min} = 4.919 \times 10^{-3} P^{\frac{1}{3}} (1 - e^2)^{\frac{1}{2}} M_*^{\frac{2}{3}} \sigma, \quad (4)$$

where, M_* , P , and e are the star mass, orbital period, and eccentricity of planet, respectively. Each signal coming from the objects include selection biases as above, which have different effects depending on the metallicities of the systems (Figure 1, (a)). Therefore, the planets in the different region of metallicity have potentially selection biases, and this effect should be considered for comparing the planetary distributions in the two metallicity regimes. Now, we made a new biased data that was filtered with the selection bias of the opposite region of metallicity in order to equalize the two selection biases in the two metallicity regions (Figure 1, (b)).

2.2. Preparing Data

The samples considered in this paper are limited to companion objects detected by radial velocity observations, allowing the orbital parameters to be characterized and the lower limit of the companion mass to be

determined. Essentially, samples are selected from those labeled “Radial Velocity” in the “detection method” column of the Extrasolar Planet Encyclopedia catalog 53 as of the end of June 2018 (Schneider et al. 2011). The radial velocities of central stars by orbiting planets, the orbital periods, and eccentricities of planets are also collected from the same catalog. On the other hand, the masses and metallicities of host stars are cited from the SWEET-Cat catalog (Santos et al. 2013; Sousa et al. 2018), and the lower limit of companion masses are calculated as below Torres et al. (2008),

$$M_p \sin i = 4.919 \times 10^{-3} P^{\frac{1}{3}} (1 - e^2)^{\frac{1}{2}} K \left(\frac{M_* + M_p}{M_{\odot}} \right)^{\frac{2}{3}}. \quad (5)$$

The radii of planets are calculated from the orbital periods and star masses. The metallicity and stellar mass are also extracted from the Casagrande catalog (Casagrande et al. 2011), the Padova database (Girardi et al. 2000), and the BaSTI stellar model (Hidalgo et al. 2018). Then, the correlation between the data from the SWEET-Cat catalog and the others was checked in order to fill up the data lacking of host stars’ masses or metallicities with linear conversion. In addition, the accuracy and term for each planetary system as indicators of selection biases were extracted from exoplanets.org. The observation term and stellar mass supply the upper limit of the maximum semi-major axis of the observable region by the radial velocity measurement for each planetary system. The maximum semi-major axis, the stellar mass and the accuracy of the radial velocity measurement were used for calculation of the lower limit on the mass of the observable planet. The other lacking data is filled up with several studies (この文章は必要か?).

The gaseous objects from all the samples used in this study are extracted in order to remove the impact of low-mass samples, such as Neptune-mass planets (gas dwarfs) and super-Earths, on this analysis. First, we determined the boundary mass between the gaseous and gas-dwarf objects from a perspective of both theory and observation. According to a previous study (Ida & Lin 2004a), gas-dwarf objects, which primarily consist of heavy-core objects such as Neptune and Uranus, have the potential to grow to the extent allowed by the core building materials inside their semi-major axes. This growth occurs via giant impacts in the inner region of the disk after the disk gas dissipates. However, this core growth is limited by the scattering effect of the heavy core increasing with greater distances from the central star. Therefore, the mass of a gas-dwarf object reaches a maximum at the semi-major axis, where the scattering effect begins to limit the core growth. Given that

the ratio of the collision-to-ejection probabilities for the heavy core is 0.1 and the core density is 1 g/cm^3 , the upper limit on the mass of a gas-dwarf object is about $0.37 M_J$. Considering a factor of the solid-angle average, the upper mass limits on a gas-dwarf object are estimated to be approximately 0.1 and $0.3 M_J$. On the other hand, a boundary between gas giants and gas dwarfs at four times the Earth's radius has been observationally revealed by the Kepler data (Buchhave et al. 2012). From the empirical planetary mass-radius relation Weiss et al. (2013), we found that the boundary of planetary mass is less than 150 times the Earth's mass and consistent with the above theoretical estimation. Based on these considerations, $0.1 M_J$ is applied in this study as the boundary mass between gas giants and gas dwarfs. Performing these preprocessing for all data observed by radial velocity observations, we use 520 planetary systems and 623 planets in this study.

3. RESULTS

In this section, we quantitatively show how different the distributions of the planets in metal-rich and -poor regions are, and where the difference comes from through classifying the samples with Gaussian Mixture Model (GMM).

3.1. Two metallicity regions

First, we determined the boundary of metallicity that divides the original samples into two such that the planetary distributions in the two regions are most different, using the method that considers the selection effects of the radial velocity measurements, as explained in Section 2.1. Figure 2 shows the p-values calculated by the AD test for the distributions of the semi-major axes and the lower limit of companion masses changing the boundary of metallicity from -0.7 to 0.4 (dex). We calculated the simulation with 1,000 iteration, and extracted the mean and standard deviation of the p-values. The minimum p-values of the AD tests for the distributions of the semi-major axes and the planet masses were 2.4×10^{-3} and $3.5 \times 10^{-5}/4.2 \times 10^{-5}$ at the metallicity of -0.04 and -0.29/-0.06 (dex), respectively; thus, the planetary distributions in the high- and low-metallicity regions do not arise from the selection effect of the radial velocity measurements but from the planet formation and evolution. In this study, we used applied -0.05 (dex) as the boundary of metallicity through considering that the two minimum p-values are around -0.05 (dex).

Second, we compared the planetary distributions on the a-Mp plane in the two regions that are divided by the boundary of metallicity. Figure 3 shows the planetary distributions and the cumulative distributions of

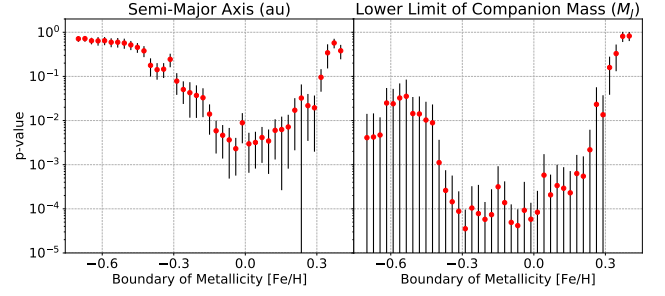


Figure 2. P-values of AD test for the semi-major axis (left) and the lower limit on the planet mass (right) of the original samples as a function of the boundary of metallicity. Red points and black vertical bars are p-values and their standard deviations calculated with 1000 iterations.

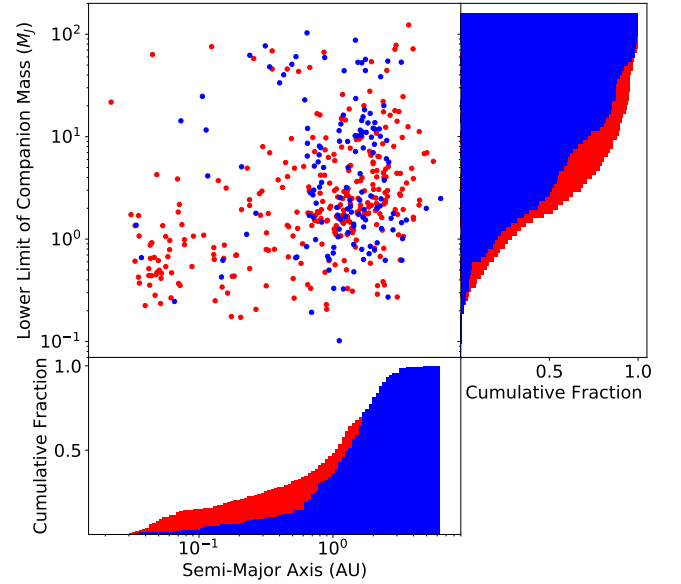


Figure 3. Planetary distributions of the semi-major axes and lower-limit of companion masses for the extracted samples in the high- and low-metallicity regions (upper left), and cumulative distributions of semi-major axis (bottom) and lower limit of companion mass (right). Red and blue points/bins represent metal-rich and -poor samples, respectively.

the semi-major axes and planet masses for the high- and low-metallicity planets. We verified that the number of the inner planets in the lower metallicity region is much smaller than that in the higher one. In addition, the number of the middle-mass planets in the lower metallicity region is smaller than that in the higher one. Thus, we found that there is no effect of the selection bias between the each metallicity region.

3.2. Three planetary-mass regimes

We classified the planetary distribution on the star-metallicity and planet-mass plane with GMM. Changing the number of the clusters as a parameter, we searched for the best model through evaluating each model with Bayesian Information Criterion (BIC), and found that the best number of the clusters for these **extracted samples** is three. Figure 4 shows the best model in the classification of the **extracted samples**.

We also investigated the eccentricity distributions of the gas giants in the metal-rich and -poor regions, where the planetary masses were divided into three populations. The tops of Figure 5 are the distributions of the eccentricities and planet mass for the **extracted samples**. The bottoms are the cumulative maps of the eccentricities for the three clusters in both the metal-rich and -poor regions. The low- and middle-mass populations distribute differently in the two metallicity regions. We evaluated the **extracted** samples of these two populations by the AD test, and found that the p-values was 5.0×10^{-5} . In contrast, the distributions of the low- and middle-mass populations in the metal-poor region are almost same. This result is consistent with the observational those that the eccentricities of massive planets in metal-rich region are potentially enhanced by planet-planet and/or planet-disk interaction (e.g., Adibekyan et al. 2013; Dawson & Murray-Clay 2013). On the other hand, the distribution of the high-mass populations in each region are almost uniform. This result means that the formation and revolution process of the gas giants over 20 M_J differs from those of the gas giants with planet mass lower than 20 M_J .

Figure 6 shows the bins plot of the host-star metallicities and eccentricities of the intermediated and massive planets. Although the intermediated planets (red bins) have the uniform eccentricities against to metallicities, the eccentricities of the massive planets are increasing as moving to high-metallicities region.

4. DISCUSSION

In this section, we compare the above results of planetary mass and eccentricity distributions with previous studies and verify the relationship. We also discuss the behavior of planetary distributions in the metal-rich and -poor regions, comparing the observed dataset from the simulation of Mordasini et al. (2012).

4.1. ?

In Mordasini et al. (2012), planets are formed by classical core accretion model, and the final semi-major axes and planetary masses are determined, based on the simulation included the planetary migration in disks and

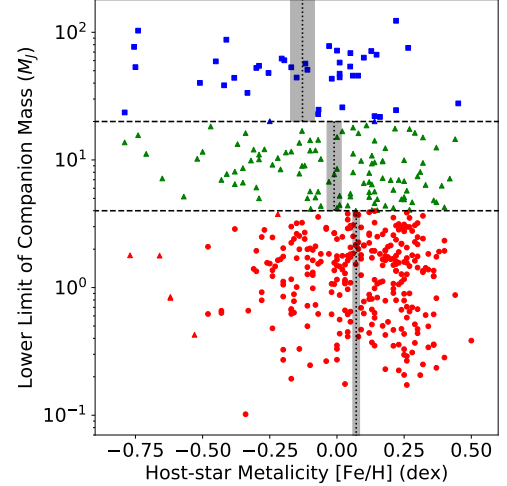


Figure 4. Distribution classified into three clusters from GMM. The samples of each cluster is described with different markers of square, triangle, and circle. The blue, green, and red points are samples divide into three fields by the mass boundaries (black horizontal lines). The black vertical lines and gray regions are the means and standard errors of metallicity in each field.

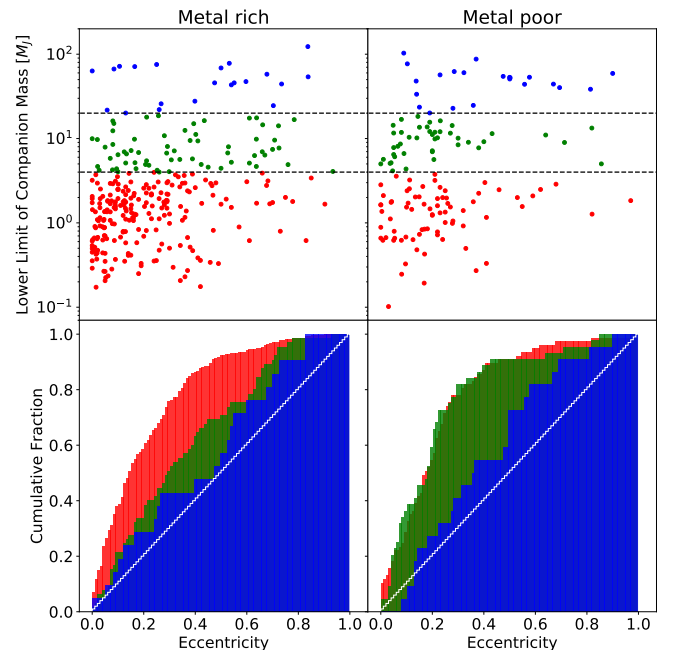


Figure 5. Distributions of the eccentricities and lower limits of companion mass (top) and the cumulative distributions of eccentricities for the gas giants in the metal-rich and -poor regions (bottom). The horizontal lines and three colors represent the same as those of Figure 4. The white steps show the distributions as uniform.

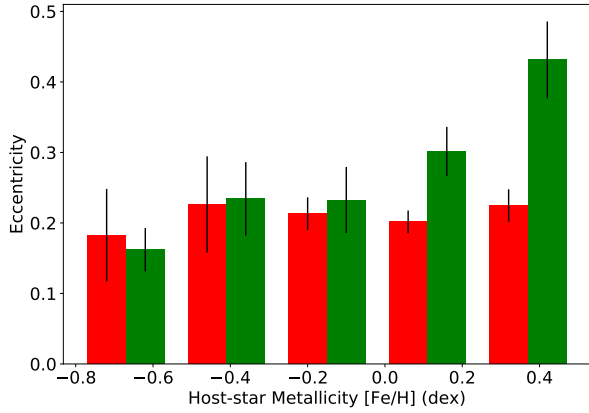


Figure 6. Bins plot of the host-star metallicities and eccentricities. The range of metallicity for each bin is 0.26 (dex), and the red and green bins represent the intermediated and massive planets, respectively. The heights and black vertical bars of each bin are the means and standard errors of the eccentricities included in each range.

the disk evolution. From our study, the two observed planetary-mass distributions, which were divided by the metal boundary, had different expanses. Then, we discuss each planetary-formation process, comparing the distribution of observed data with that of simulation data. Figure 7 shows that the comparison between the observed data included the selection biases and simulation data cited from Mordasini et al. (2012). The simulation data were also filtered by both selection biases of metal-rich and -poor regions to complete the conditions with the observed data. As the result, the distributions of metal rich regions are very consistence, which can explain that most of gas giants in the metal rich region are formed by core accretion. This is also explained by our results shown in Section ?? because of below interpretation. The interaction between a gas giant and protoplanetary disk possibly makes the eccentricity of planet grow (Goldreich & Sari 2003; Kley & Dirksen 2006). This interaction is concentrated at discrete Lindblad and corotation resonances, which causes the planet’s orbit to migrate and open a gap in the disk as the planet mass is large enough. If the viscous coefficient equals to 10^{-5} , the planet with circular orbit changes to eccentric orbit as the planetary mass is over $3 M_J$. The more massive planets make their eccentricity higher until the maximum value 0.25. On the other hand, if a planetary system has two gas giants, the outer planet may prolong the orbital period of the inner planet. These planets’ eccentricities grow up in rough inverse proportion to their masses by this orbital

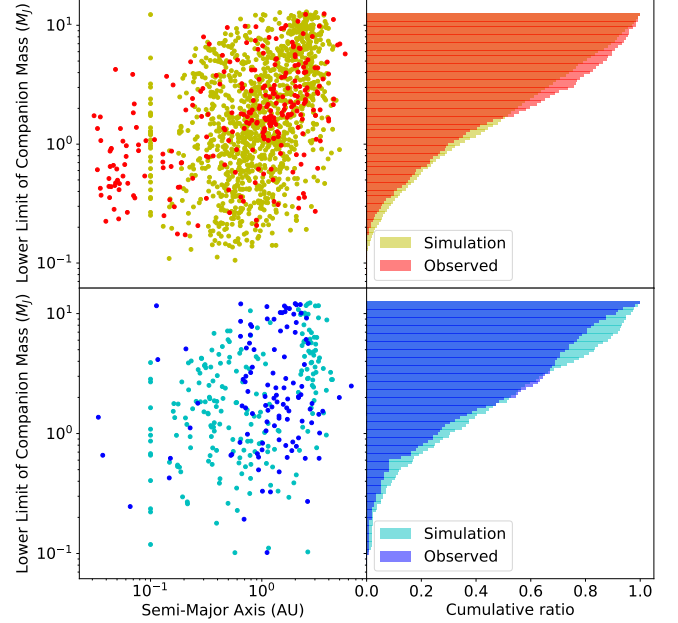


Figure 7. Comparison of planetary distributions between the observed data (red and blue points) and simulation data (yellow and cyan points) in the metal-rich region (upper left) and the metal-poor region (lower left), and the cumulative maps of planetary masses in the metal-rich region (upper right) and the metal-poor region (lower right).

interaction (Chiang et al. 2002). From the verification of simulation (Ida et al. 2013), gas giants and rocky/icy planets emerge, migrate, and undergo dynamical instability in a relatively massive disk, and the perturbation between planets causes orbital crossing, eccentricity excitation, and planetary ejection. Therefore, gas giants formed through core accretion tend to have high eccentricities, which is consistent to our results of eccentricity distribution.

In contrast, the distributions of metal poor regions between the observed data and the simulation data are different. This means that the planetary formation process in metal poor disks differs from in metal rich disks: the planetary formation in metal poor region cannot be explained by only core accretion. On the other hand, the eccentricity of gas giant formed via disk instability ranges from 0 to 0.35 in initial stage, and decreases as the planet mass increases (Boss 2011). Note that the range of semi-major axis is $30 \sim 70$ au. This trend can be also seen slightly in the metal poor region of Figure 5. However, because it is not clear, there possibly exists other formation processes included core accretion in metal poor regions.

4.2. ?

According to previous studies, the planetary distributions are divided into two regions. Host stars over $4 M_J$ tend to be more metal poor and massive, but below this value show the well-known metallicity-giant planet frequency correlation (Santos et al. 2017). In addition, planets formed through core accretion have upper bound of mass, which equals around $10 M_J$, and planets over this value likely formed through gravitational disk instability (Schlaufman 2018). However, we show that the planetary distribution has multiple regions depending on planetary mass and disk metallicity. Figure 8 shows that the planetary distribution used in this study. The colors of red and blue mean the planets in metal rich

and poor regions, respectively. The markers describe the different ranges of planet mass, which divided with mass boundary determined by the classification in Section 3.2.

According to previous studies, the distribution of gas-giant masses can be divided into two regions by the border of $4 M_J$ with metallicity bias, which insists that the planetary-formation processes in each region are different (e.g., Santos et al. 2017). In contrast, the boundaries were drawn at 4 and $20 M_J$ from our result, which the former is consistent with the previous studies. The latter indicates the border between the gas giants and brown dwarfs.

REFERENCES

- Adibekyan, V. Z., Figueira, P., Santos, N. C., et al. 2013, *A&A*, 560, A51
- Boss, A. P. 1997, *Science*, 276, 1836
- Boss, A. P. 2002, *ApJL*, 567, L149
- Boss, A. P. 2011, *ApJ*, 731, 74
- Buchhave, L. A., Latham, D. W., Johansen, A., et al. 2012, *Nature*, 486, 375
- Cai, K., Durisen, R. H., Michael, S., et al. 2006, *ApJL*, 636, L149
- Casagrande, L., Schönrich, R., Asplund, M., et al. 2011, *A&A*, 530, A138
- Chiang, E. I., Fischer, D., & Thommes, E. 2002, *ApJL*, 564, L105
- Dawson, R. I., & Murray-Clay, R. A. 2013, *ApJL*, 767, L24
- Dupuy, T. J., & Liu, M. C. 2011, *ApJ*, 733, 122
- Durisen, R. H., Reipurth, V., Jewitt, K., et al. 2007, *Univ. of Arizona Press, Tucson* 951, 607-622
- Fischer, D. A., & Valenti, J. 2005, *ApJ*, 622, 1102
- Girardi, L., Bressan, A., Bertelli, G., & Chiosi, C. 2000, *A&AS*, 141, 371
- Goldreich, P., & Sari, R. 2003, *ApJ*, 585, 1024
- Hayashi, C., Nakazawa, K., & Nakagawa, Y. 1985, *Protostars and Planets II*, 1100
- Hidalgo, S. L., Pietrinferni, A., Cassisi, S., et al. 2018, *ApJ*, 856, 125
- Ida, S., & Lin, D. N. C. 2004, *ApJ*, 604, 388
- Ida, S., & Lin, D. N. C. 2004, *ApJ*, 616, 567
- Ida, S., Lin, D. N. C., & Nagasawa, M. 2013, *ApJ*, 775, 42
- Kley, W., & Dirksen, G. 2006, *A&A*, 447, 369
- Kuiper, G. P. 1951, *Proceedings of the National Academy of Science*, 37, 1
- Lee, K. J., Guillemot, L., Yue, Y. L., Kramer, M., & Champion, D. J. 2012, *MNRAS*, 424, 2832
- Ma, B., & Ge, J. 2014, *MNRAS*, 439, 2781
- Matsuo, T., Shibai, H., Ootsubo, T., & Tamura, M. 2007, *ApJ*, 662, 1282
- Mayor, M., & Queloz, D. 1995, *Nature*, 378, 355
- Mayer, L., Quinn, T., Wadsley, J., & Stadel, J. 2002, *Science*, 298, 1756
- Mayer, L., Lufkin, G., Quinn, T., & Wadsley, J. 2007, *ApJL*, 661, L77
- Mayor, M., Marmier, M., Lovis, C., et al. 2011, *arXiv:1109.2497*
- Mizuno, H. 1980, *Progress of Theoretical Physics*, 64, 544
- Mordasini, C., Alibert, Y., Benz, W., & Naef, D. 2009, *A&A*, 501, 1161
- Mordasini, C., Alibert, Y., Benz, W., Klahr, H., & Henning, T. 2012, *A&A*, 541, A97
- Perri, F., & Cameron, A. G. W. 1974, *Icarus*, 22, 416
- Pollack, J. B., Hubickyj, O., Bodenheimer, P., et al. 1996, *Icarus*, 124, 62
- Ribas, I., & Miralda-Escudé, J. 2007, *A&A*, 464, 779
- Santos, N. C., Israelian, G., Mayor, M., Rebolo, R., & Udry, S. 2003, *A&A*, 398, 363
- Santos, N. C., Sousa, S. G., Mortier, A., et al. 2013, *A&A*, 556, A150
- Santos, N. C., Adibekyan, V., Figueira, P., et al. 2017, *A&A*, 603, A30
- Schlaufman, K. C. 2018, *ApJ*, 853, 37
- Schneider, J., Dedieu, C., Le Sidaner, P., Savalle, R., & Zolotukhin, I. 2011, *A&A*, 532, A79
- Sousa, S. G., Adibekyan, V., Delgado-Mena, E., et al. 2018, *A&A*, 620, A58

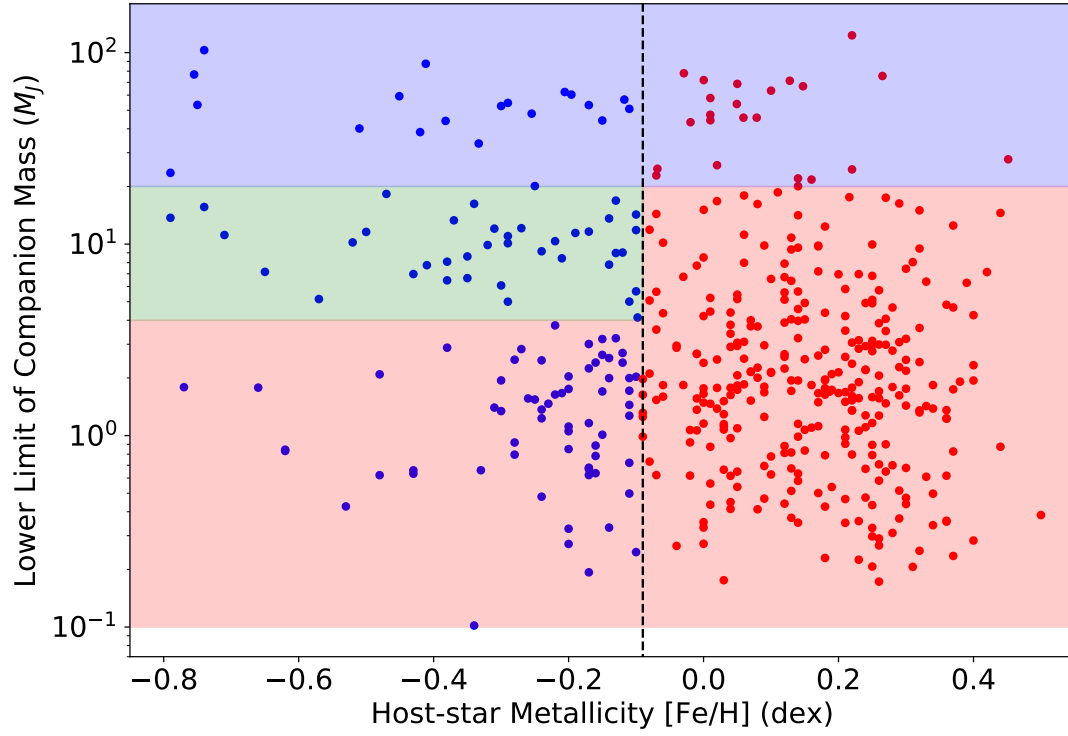


Figure 8.

Tanigawa, T., & Tanaka, H. 2016, ApJ, 823, 48

Torres, G., Winn, J. N., & Holman, M. J. 2008, ApJ, 677,
1324

Wang, J., & Fischer, D. A. 2015, AJ, 149, 14

Weiss, L. M., Marcy, G. W., Rowe, J. F., et al. 2013, ApJ,
768, 14